Journal of Electroceramics 6:1, 27–41, 2001

Conduction and Gas-Surface Reaction Modeling in Metal Oxide Gas Sensors

BRIAN CHWIEROTH[1], BRUCE R. PATTON[1], & YUNZHI WANG[2]
Center for Industrial Sensors and Measurements, The Ohio State University, Columbus, OH 43210

Submitted July 2, 1999; Revised August 10, 2000; Accepted September 22, 2000

Abstract. A phenomenological approach to the operation of metal oxide gas sensors, the Integrated Reaction Conduction (IRC) model, is proposed which integrates the gas-surface reactions with the electrical conduction process in a weakly sintered, porous metal oxide. An effective medium approximation is employed to relate the mesoscopic microstructure and the carrier depletion at the granular surface to the macroscopic electrical conduction. For a given ambient gas concentration and temperature, the electron concentration in the depletion layer is calculated from the gas-surface reaction kinetics. The adsorption and oxidation reaction energies of the gas sensing reactions are extracted for a TiO_{2-x} CO sensor by comparing experimental data with three-dimensional plots of IRC model resistance as a function of the ambient [CO(g)] and temperature. The IRC model predicts novel properties of the gas sensor, including the sensitivity and the response range, which depend on the doping of the sensor material, the temperature, the grain size, and the geometry of the necks between grains.

Keywords: gas sensors, modeling, electrical conduction, gas-surface reactions, effective medium theory

I. Introduction

Research pursuing the development of gas sensors for high temperature harsh industrial environments (>400°C) found in the aerospace and automotive industries has centered on non-stoichiometric semiconductive metal oxides such as TiO_2 and SnO_2 [1,2]. Gas sensors made from these materials have the desirable property that their resistance depends strongly on the adsorption of certain gases [3]. Although both n-type and p-type semiconductors are known to function as sensors, the n-type semiconductors have more often been utilized because the p-type oxides are relatively unstable to the exchange of lattice oxygen with air [4]. In particular, for non-doped TiO_{2-x}, which is n-type in both anatase and rutile phases above 400°C [5], the defect formation energies of both oxygen vacancies (Schottky type disorder) and interstitial titanium atoms (Frenkel type) are large compared to k_BT [6–10].

In the standard picture for a weakly sintered polycrystalline n-type semiconducting sensor (*e.g.* TiO_{2-x}, SnO_2, ZnO), ambient oxygen adsorbs on the surfaces of the grains, and forms negative oxygen ions (mainly O^- at >400°C [11]) by combining with intrinsic electrons from the semiconductor [12]. This produces a dipole layer associated with the charged surface and a corresponding depletion region inside the surface of the grain, resulting in a highly resistive intergranular contact. If the grains are small in size compared to the depletion layer width, the high resistivity region may well extend throughout the grain.

Sensing takes place when the surface resistance is lowered in a process in which a reducing agent such as carbon monoxide (CO) reacts with the surface oxygen ions, re-injecting electrons into the oxide interior and decreasing the width of the depletion layer. SnO_2 and ZnO based CO sensors have previously been observed

[1]Department of Physics and [2]Department of Materials Science and Engineering,

to follow this mechanism [13,14]. The n-type sensor, therefore, may be viewed as a medium consisting of two regions of widely differing conductivity, in which electrical conduction is modulated by changing the volume fraction of the highly conducting granular interior through reaction with an adsorbed gas.

To optimize sensor performance, a detailed theoretical model is needed which incorporates the complete range of phenomena comprising the effects of gas-surface reactions on sensor conductance. This model must include the kinetics of the gas-surface reaction chemistry, the relation of the surface reactions to changes in the depletion layer width, and the effect of the intergranular resistance on the electrical conduction through the multicomponent material.

In this paper we develop such a phenomenological modeling approach, the Integrated Reaction Conduction (IRC) model, which integrates the various states and length scales of the sensing processes that contribute to the macroscopic response of the gas sensor. Following previous industrial successes in which computer-aided modeling has improved the design of semiconductor devices [15], the IRC model facilitates sensor optimization by predicting the behavior of the gas sensor as a function of the ambient gas concentration, the temperature, the addition of dopants, differing grain sizes, and the intergranular contacts developed during sintering. Realistic weakly sintered porous microstructures derived from phase field calculations [16] are used to develop a re-normalized effective medium conductivity model of the sintered ceramic, while the surface reactions are described in a simple adsorption-oxidation process which controls how the subsequent re-injected electrons modify the electrical conduction. As an example of the facility and accuracy of the IRC model, the reaction energies of CO gas adsorption and oxidation on a reduced TiO_{2-x} ceramic are extracted from experimental data [17].

Our approach is organized in the following sections. In section II we discuss the modeling of the electrical transport in the sensor using an effective medium theory for the microstructure, while the gas-surface reaction calculations are presented in section III. Section IV compares the theoretical results from the IRC model with experiment, and considers the results of varying the reaction energies through impurity doping. Using the IRC model, in Section V we predict further sensor optimization through reduced grain sizes and increased neck sizes of the intergranular contacts. Finally a summary is presented in section VI.

II. Electrical Transport in Granular Metal Oxide: Effective Medium Approximation

The microscopic treatment of the surface impedance caused by the depletion layer requires consideration of the type of contact formed during sintering at the interface between two grains. The intergranular contacts in the weakly sintered microstructure to which we compare the IRC model are dominated by the formation of back-to-back Schottky barriers [17]. Often this surface impedance is temperature dependent and is, in some cases, also nonlinear [18]. Details of these dependencies and their relation to the metal oxide band structure and adsorbed surface oxygen ions will be considered separately.

Intergranular Schottky barriers are formed during the sintering of the samples in air, prior to CO exposure. The depletion of free electrons near the grain surfaces results from the reaction of adsorbed surface oxygen to form O^-, according to the scenario described in the introduction. During the actual CO sensing experiments, operated under conditions of controlled nitrogen atmosphere, oxygen impurities occur at minimal levels of parts-per-million in the ambient nitrogen/CO gas stream [17]. Consequently, the Schottky barrier height may reasonably be expected to remain constant throughout the sensing measurements, as the nitrogen background is inert with respect to the oxide. Therefore, in the present work we use a simpler approach (Fig. 1) to characterize the essential features of the interface during the sensing process. We associate a small constant conductivity with the depletion layer region near the surface of the oxide grains and a large constant conductivity with the inte-

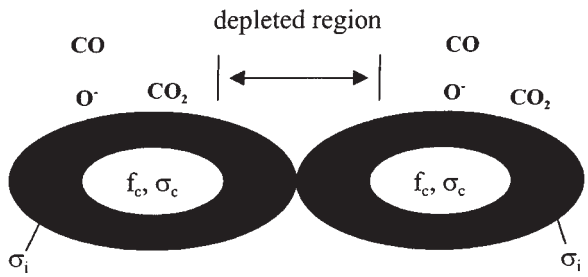

Fig. 1. The physical sensing process in the IRC model. Sensing occurs via a surface oxidation reaction between adsorbed CO and surface oxygen ions, forming CO_2 and re-injecting electrons into the depletion layer, decreasing its width. The depletion layer region has a small conductivity σ_1, compared to the large conductivity σ_c of the bulk interior region (volume fraction f_c).

rior region (in the case where the grain is not fully depleted).

Since we are primary interested here in novel features which arise from the integrated modeling across a wide range of length scales, for our purposes the essential percolative behavior of the effective conductivity of the two component medium may be reasonably well described by an effective medium theory (EMT). In the present case the high conductivity interior regions are dispersed within low conductivity (depletion and grain boundary) regions. For a three-dimensional sample, the effective conductivity for such a coated two component mixture is given by the Bruggeman unsymmetrical EMT [19]

$$\frac{(\sigma_{\text{eff}} - \sigma_c)^3}{\sigma_{\text{eff}}} = (1 - f_c)^3 \frac{(\sigma_i - \sigma_c)^3}{\sigma_i} \qquad (1)$$

where σ_i and σ_c are the conductivities of the insulating and conducting components, respectively, and f_c is the volume fraction of the high conductivity interior component (the non-depleted regions of the grain). The ratio σ_i / σ_c may be calculated from the Schottky barrier height of the grain-grain contacts and is taken as a constant in this paper.

Because conduction paths through the material must always go through the insulating Schottky contact regions, the low conductivity and high conductivity regions are always effectively in series for any composition f_c [20]. The insulating component coating the grains thus has a controlling effect on the conduction and keeps the effective conductivity from approaching the high conductivity of the bulk interior until the fraction of insulating component approaches zero (see Fig. 2). In the sensor, this would in principle occur when complete reaction with a reducing gas has removed all ionized oxygen from the surface and returned the 'missing' carriers to the depletion layer, resulting in a one-component medium of conductivity σ_c with f_c equal to one.

To accurately quantify the effective conductivity in the two component granular material, an explicit mapping must be developed to relate the macroscopic effective medium picture with the more detailed mesoscopic treatment of grains, grain boundaries and voids. Such a mapping obviously depends on details of the microstructure which include grain size and orientation, grain boundary thickness and connectivity, and pore fraction and distribution. We use a phase field model to obtain the essential features of the microstructure of a weakly sintered composite [16]. The phase field method offers a number of unique features. First, it can easily describe an arbitrary morphology of a complex microstructure by using the field variables. Secondly, it can take into account various thermodynamic driving forces responsible for the microstructural evolution. Third, the diffusion equation allows a straightforward characterization of various long-range diffusion processes that dominate during sintering. Finally, the time, length and temperature scales in the phase field method are determined by the semi-phenomenological constants used in the time dependent evolution equations which can, in principle, be related to experimentally measured or *ab initio* calculated quantities for a particular system. Therefore, this method can be directly applied to real material systems. These features, which make the phase field approach an attractive method in dealing with microstructural evolution in a wide range of materials processes, have been discussed recently [21].

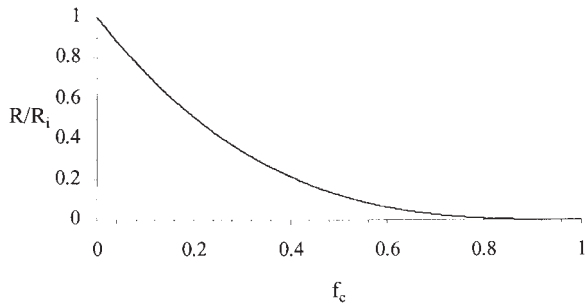

Fig. 2. Resistance R of the coated two-phase mixture vs. fraction of bulk conducting component f_c, as given by the Bruggeman unsymmetrical effective medium theory for $R_c/R_i = 10^{-3}$. R_i is the resistance of the insulating depletion layer, and R_c is the bulk interior resistance. The coating insulating component has a controlling effect on R such that R does not equal R_c until f_c equals one.

From the phase field microstructure (Fig. 3) we identify the interior grain volume V_{gi}, the grain boundary volume V_{gb} (including the depletion layer), and the volume of pores in both the interior of grains V_{pg}, and at the grain boundary V_{pgb}. The two pore volumes make up the total void fraction in a simulation. If the volume of the sample is V_s, then the relative fractions associated with the interiors of grains, grain boundary-depletion layer, pores inside grains, and pores at grain boundaries can be defined as $f_g = V_{gi}/V_s$, $f_{gb} = V_{gb}/V_s$, $f_{pg} = V_{pg}/V_s$, $f_{pgb} = V_{pgb}/V_s$, respectively, which satisfy the condition $f_g + f_{gb} + f_{pg} + f_{pgb} = 1$.

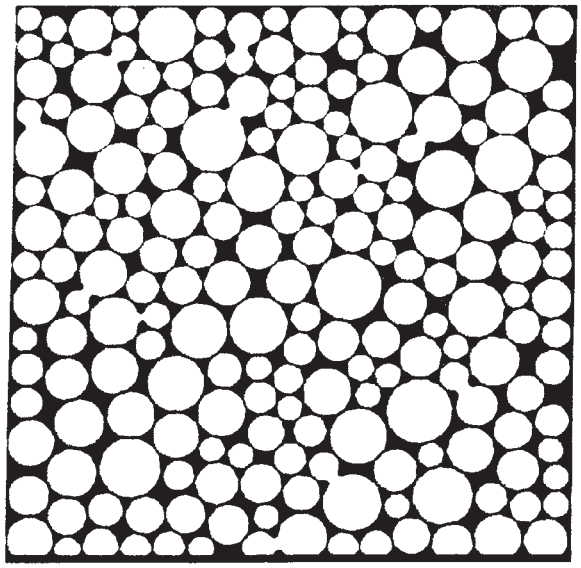

Fig. 3. A typical example of the granular microstructure simulated by the phase field method. The details of neck geometry at the early stages of sintering are shown.

Thus we may describe the correlated mesoscopic structure with an effective conductor fraction which is the sum of the grain fraction and the included pore fraction within the grain, $f_c = f_g + f_{pg}$. Similarly, we may identify the insulator fraction f_i as the sum of the grain boundary and grain boundary pore fractions, $f_i = f_{gb} + f_{pgb}$.

Because voids introduce regions of zero conductivity both in the bulk conducting and coating insulating regions, the effective conductivities of the insulating and conducting components are reduced. In the interior of a grain, the effects of voids are accurately described by the same unsymmetrical EMT discussed above, such that the effective bulk interior conductivity is not the original grain conductivity σ_g, but the re-normalized value given by $\sigma_m = \sigma_g (1 - f_{pg})^{3/2}$. To determine the re-normalized conductivity associated with the grain boundary, we note that pores block electrical transport between adjoining grains. Since the interfacial regions are in series with the conducting grains, the pores effectively reduce the interfacial conductivity in proportion to the cross-sectional area of the sample that is occupied by the grain boundary pores. Thus we may describe the interfacial region by an effective conductivity σ_i which is related to the mean-field grain boundary-depletion layer conductivity σ_{gb} by the relation $\sigma_i = \sigma_{gb} (1 - f_{pgb}^{2/3})$.

The unsymmetrical EMT result from Eq. (1), together with the equations for the volume fractions f_c and f_i and the effective conductivities σ_c and σ_i, constitute a mapping of the mesoscopic results of the field kinetic modeling onto the effective medium model at the macroscopic level (see flow chart in Fig. 4). The pore volume fractions are determined from the phase field model of the microstructure and are constant throughout the simulation. Grain and grain boundary volume fractions, however, change upon exposure to a reducing gas, and are determined using the chemical kinetic methods discussed in the next section.

III. Calculating f_g and f_{gb}: Gas-Surface Reactions

The oxidation of a reducing gas like CO takes place, as discussed in Section I, by a series of reactions in which CO is first adsorbed onto the metal oxide surface, then reacts with O^- oxygen ions to form CO_2 and liberate electrons. Prior to the introduction of carbon monox-

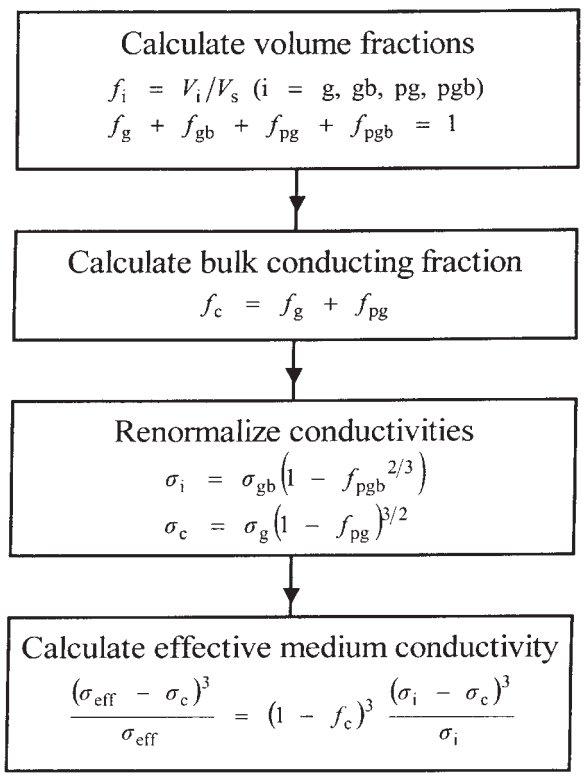

Fig. 4. Flow chart summarizing the relation of the mesoscopic microstructure to the macroscopic effective medium conductivity (see text for variable definitions).

ide gas, the depletion layer volume fraction f_{gb} is determined by the number of intrinsic free electrons N_i depleted by N_d surface oxygen ions according to

$$f_{gb} = f_{np}\left(\frac{N_d}{N_i}\right), \quad (2)$$

where $f_{np} = 1 - f_{pg} - f_{pgb}$ is the total non-pore volume fraction. N_i is related to the intrinsic non-stoichiometry x; for example, in n-type TiO_{2-x}, $N_i = 2x\rho V_g$, where ρ is the number of molecular TiO_2 units per unit volume, and V_g the volume of the grain. Similarly, N_d is proportional to the number of oxygen ions per surface area $[O^-_{ads}]$ via the product $[O^-_{ads}]A_g$, where A_g is the surface area of the grain. Furthermore, N_d and N_i satisfy the relation $N_d \leq N_i$, with full depletion of the grain occurring for $N_d = N_i$. After exposure to the reducing gas, the N_{lib} electrons liberated by the oxidation reaction return to the grain and increase the volume fraction f_g of the conducting interior to

$$f_g = f_{np} - f_{gb} = f_{np}\left(\frac{N_i - N_d + N_{lib}}{N_i}\right), \quad (3)$$

Despite oxygen impurities at the level of parts-per-million in the ambient nitrogen/CO gas stream, the equilibrium defect concentration x in the TiO_{2-x} lattice is essentially unchanged throughout the sensing process. This is because in TiO_{2-x} it is energetically more favorable for an adsorbed oxygen to form a surface O^- with an ionization energy ~ 0.7 eV [22], rather than fill in an oxygen vacancy defect with a formation energy ~ 2.1 eV [8]. Nevertheless, the ambient O_2 gas concentration is an important variable in determining both the intrinsic defect concentration and the bulk conductivity of the oxide. In the present work, as a reasonable first approximation, we consider only the behavior at fixed carrier concentration, and will consider the effect of O_2 gas concentration separately. Accordingly, in equilibrium x, and therefore N_i, are in essence constant during the sensing measurement relative to the more significant changes in the other two terms in Eq. (3). The scope of the depletion layer is thus parameterized by the concentrations of surface O^- ions $[O^-_{ads}]$ and liberated electrons $[e^-_{lib}]$, where $[e^-_{lib}]V_g = N_{lib}$.

Next we consider alternative models for the gas-surface reactions that lead to the increased electron concentration in the depletion layer. We seek the most straightforward description of the sensing mechanism that also elucidates the functional intricacies observed in the experimental data. We consider first a picture that uses two separate reactions for the adsorption of CO and its subsequent oxidation reaction with the O^- ions.

1. Two-reaction Energy Model

Starting with an adsorbed layer of O^- on the oxide surface, the adsorption and oxidation equilibrium reactions that contribute to the overall CO sensing mechanism are [23]

$$CO(g) + O^-_{ads} \underset{k_{ads,r}}{\overset{k_{ads,f}}{\leftrightarrow}} CO_{ads}\cdot O^-_{ads} \underset{k_{ox,r}}{\overset{k_{ox,f}}{\leftrightarrow}} CO_{2,ads} + e^-_{lib} \quad (4)$$

where $k_{ads,f}$, $k_{ads,r}$, $k_{ox,f}$, $k_{ox,r}$ are the forward and reverse reaction rates of adsorption and oxidation. Because the number of CO_2 molecules forming on the oxide surface equals the number of liberated electrons replenishing the depletion layer, determining an expression for $[CO_{2,ads}]$ is equivalent to calculating $[e^-_{lib}]$. We assume that ambient CO_2 impurities are negligible [17].

The changing reactant concentrations resulting from exposure of the oxide to the reducing gas may be expressed in terms of the sensing mechanism reaction rates [24].

$$\frac{d[CO(g)]}{dt} = k_{ads,r}[CO_{ads}\cdot O^2_{ads}] - k_{ads,f}[CO(g)]\cdot[O^2_{ads}] \quad (5a)$$

$$\frac{d[CO_{ads}\cdot O^-_{ads}]}{dt} = k_{ads,f}[CO(g)]\cdot[O^-_{ads}] - k_{ads,r}[CO_{ads}\cdot O^-_{ads}] - k_{ox,f}[CO_{ads}\cdot O^-_{ads}] + k_{ox,r}[CO_{2,ads}] \quad (5b)$$

$$\frac{d[CO_{2,ads}]}{dt} = k_{ox,f}[CO_{ads}\cdot O^-_{ads}] - k_{ox,r}[CO_{2,ads}] \quad (5c)$$

The time derivatives in Eqs. (5) vanish for the case of steady state resistance measurements [17]. The steady state concentrations of $CO_{2,ads}$ and O^-_{ads} are thus

$$[CO_{2,ads}] = \frac{k_{ads,f}}{k_{ads,r}}\frac{k_{ox,f}}{k_{ox,r}}[CO(g)][O^-_{ads}] \quad (6a)$$

$$[O^-_{ads}] = \frac{[CO_{ads} \cdot O^-_{ads}]}{\frac{k_{ads,f}}{k_{ads,r}}[CO(g)]} \tag{6b}$$

Since $[CO_{ads} \cdot O^-_{ads}]$ is not readily obtainable experimentally, in order to express Eqs. (6) in a more practical form we use a conservation law governing the occupation of surface sites:

$$[O^-_{ads}] + [CO_{ads} \cdot O^-_{ads}] + [CO_{2,ads}] = [S_o], \tag{7}$$

where $[S_0]$ is the concentration of O^- ion adsorption sites on a ceramic grain. Invoking Eq. (7) and the appropriate relation between $[CO_{2,ads}]$ and $[e^-_{lib}]$, the steady state concentrations of e^-_{lib} and O^-_{ads} are

$$[e^-_{lib}] = \frac{[CO_{2,ads}]A_g}{V_g} = \frac{\frac{k_{ads,f}}{k_{ads,r}}\frac{k_{ox,f}}{k_{ox,r}}[CO(g)]\cdot[S_o]}{1+\left(\frac{k_{ox,f}}{k_{ox,r}}\right)\frac{k_{ads,f}}{k_{ads,r}}[CO(g)]}\frac{A_g}{V_g} \tag{8a}$$

$$[O^-_{ads}] = \frac{[S_o]}{1+\left(\frac{k_{ox,f}}{k_{ox,r}}\right)\frac{k_{ads,f}}{k_{ads,r}}[CO(g)]} \tag{8b}$$

The ratios of the forward and reverse reaction rates in Eqs. (8) are simplified by evaluating the partition function of each reaction participant (or alternatively by solving the master equation)

$$\frac{k_f}{k_r} = \frac{Z_{product}}{Z_{reactant}} e^{-E/k_BT} \tag{9}$$

where E is the difference between the activation energies of the forward and reverse reactions ($E = E_f - E_r$) [25,26], or equivalently, the difference between the energy levels of the steady state reaction participants, which we define in this paper as the reaction energy (see Fig. 5a). We denote by E_{ads} the reaction energy between adsorbed and non-adsorbed CO (the adsorption reaction), and by E_{ox} the reaction energy between adsorbed CO and CO_2 (the oxidation reaction).

In evaluating the steady state properties of the sensor, we note that the partition function ratio $Z_{product}/Z_{reactant}$ for the adsorption reaction is the cubic power of the Debye wavelength $\lambda_{CO(g)}$ for CO gas

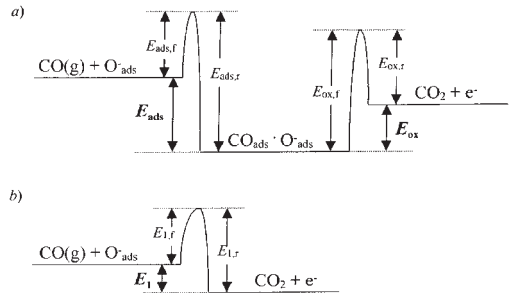

Fig. 5. Reaction energies for *a*) two-reaction energy model, and *b*) one-reaction energy model. The reaction energy (E_{ads}, E_{ox}, or E_1) is the respective difference between the activation energies of the forward and reverse reactions (E_f and E_r), or equivalently, the difference between the energy levels of the steady state reaction participants.

(equal to 1.19×10^{-11} m at 500°C), and unity for the oxidation reaction. Therefore, the reaction rate ratios in Eqs. (8) equal

$$\frac{k_{ads,f}}{k_{ads,r}} = \lambda^3_{CO(g)} \exp\left[-\frac{E_{ads}}{k_BT}\right] \tag{10a}$$

$$\frac{k_{ads,f}}{k_{ads,r}} = \exp\left[-\frac{E_{ox}}{k_BT}\right] \tag{10b}$$

Both the concentration of liberated electrons $[e^-_{lib}]$ and the surface ion concentration $[O^-_{ads}]$ are now simply expressed in terms of the reaction energies of the sensing mechanism (4), the CO gas concentration, the ion adsorption site concentration, and the grain surface area to volume ratio. Together with the relations for N_{lib} and N_d, the concentrations $[e^-_{lib}]$ and $[O^-_{ads}]$ determine f_g via Eq. (3). Using the IRC model, the reaction energies for carbon monoxide gas adsorption and oxidation on a reduced ceramic sensor can be extracted from experimental data. In addition, the IRC model, via Eqs. (8), elucidates the functional role of the reaction energies and grain size in the sensor response.

2. One-reaction Energy Model

We now investigate the possibility of describing the surface gas reactions with a simpler model of the sensing process that combines the adsorption and oxidation stages into a single-stage sensing mechanism, as suggested in the literature [13,14]

$$\mathrm{CO(g)} + \mathrm{O}^{-}_{\mathrm{ads}} \underset{k_{\mathrm{l,r}}}{\overset{k_{\mathrm{t,f}}}{\leftrightarrow}} \mathrm{CO}_{2,\mathrm{ads}} + e^{-}_{\mathrm{lib}} \tag{11}$$

Using the same methodology described above for the two-stage sensing process, the concentrations $[\mathrm{O}^{-}_{\mathrm{ads}}]$ and $[e^{-}_{\mathrm{lib}}]$ which determine the depletion layer volume fraction are given by

$$[e^{-}_{\mathrm{lib}}] = \frac{[\mathrm{CO}_{2,\mathrm{ads}}]}{V_{\mathrm{g}}} = \frac{\dfrac{k_{\mathrm{l,f}}}{k_{\mathrm{l,r}}}[\mathrm{CO(g)}][\mathrm{S_o}]}{1 + \dfrac{k_{\mathrm{l,f}}}{k_{\mathrm{l,r}}}[\mathrm{CO(g)}]} \frac{A_{\mathrm{g}}}{V_{\mathrm{g}}} \tag{12a}$$

$$[\mathrm{O}^{-}_{\mathrm{ads}}] = \frac{[\mathrm{S_o}]}{1 + \dfrac{k_{\mathrm{l,f}}}{k_{\mathrm{l,r}}}[\mathrm{CO(g)}]} \tag{12b}$$

$$\frac{k_{\mathrm{l,f}}}{k_{\mathrm{l,r}}} = \mu^{3}_{\mathrm{CO(g)}} \exp\left[\frac{-E_{\mathrm{l}}}{k_{\mathrm{B}}T}\right] \tag{12c}$$

where $k_{\mathrm{l,f}}$ and $k_{\mathrm{l,r}}$ are the forward and reverse reaction rates of sensing mechanism (11), and E_1 ($E_1 = E_{\mathrm{l,f}} - E_{\mathrm{l,r}}$) is the reaction energy (see Fig. 5b). The liberated electron and surface O^{-} concentrations produced by the single-reaction energy model will be used together with Eqs (1) and (3) to examine whether this simpler mechanism is a viable alternative to the two-stage model.

IV. Comparison with Experiment

The effective conductivity of the reduced titania sensor is calculated as a function of the CO gas concentration and temperature from the two-stage IRC model by substituting Eqs. (3), (8) and (10) into Eq. (1). The results determined by the IRC model (lighter continuous grid in Fig. 6) demonstrate the qualitatively correct behavior of an n-type gas sensor, that is, the resistance R of the two component composite decreases from its initial resistance R_{o} at 0% CO gas concentration when exposed to the reducing gas. Moreover, by comparing three-dimensional plots of IRC model resistance as a function of the ambient gas concentration and temperature to experimental data, the IRC model is able to extract the adsorption and oxidation reaction energies of the gas sensing reactions. Fig. 6 shows that, for $E_{\mathrm{ads}} = -0.34$ eV and $E_{\mathrm{ox}} = 0.22$ eV, the IRC model resistance (lighter continuous grid) matches the experimentally measured resistance (dark line segments connect data points) of a pure anatase TiO_{2-x} CO sensor in a nitrogen ambient background for a temperature range 673 K − 873 K (400°C − 600°C) [17]. The negative value for the reaction energy E_{ads} signifies, by its definition, that the activation energy for CO adsorption is less than the desorption activation barrier. We have compared the IRC model to this data assuming the sensor possesses a weakly sintered microstructure with Schottky barrier intergranular contacts, and

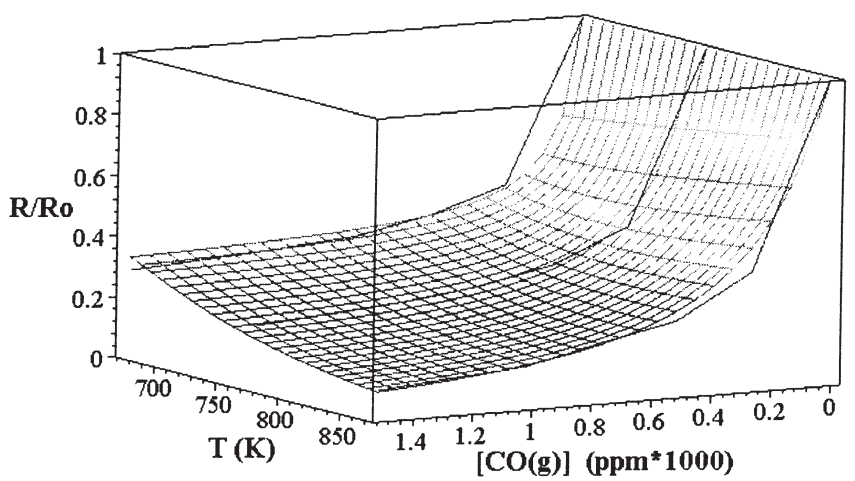

Fig. 6. IRC model resistance R (lighter continuous grid) as a function of temperature T and CO concentration for a weakly sintered, coarse-grained TiO_{2-x} sensor compared to experimental data (dark line segments connect data points) for T ranging from 673 − 873 K (400°C − 600°C) [17]. R_{o} is the resistance at 0% CO gas concentration. Using two-reaction energy IRC modeling, the reaction energies $E_{\mathrm{ads}} = -0.34$ eV and $E_{\mathrm{ox}} = 0.22$ eV are extracted from the data.

coarsened grains sufficiently large compared to the depletion layer to allow for a non-zero initial bulk conducting fraction [17]. The reaction energies (Table 1) found for the anatase-phase based sensors are characteristic of those reported for CO physisorption [27] and the O^- ionization reaction [28]. The IRC model is therefore valuable in extracting the gas-surface reaction kinetics that contributes to the operation of metal oxide gas sensors.

Though the changes in E_{ads} and E_{ox} due to the addition of La_2O_3 and CuO shown in Table 1 are less than one-tenth eV, these variations significantly alter the response properties of the gas sensor. Figs. 7 and 9 show calculated resistances using reaction energies differing by hundredths of eV from those extracted for the pure anatase sensor shown in Fig. 6. Comparison of these plots demonstrates that small alterations in the reaction energies produce considerable changes in the response range and the sensitivity. The variations in the reaction energies obtained by two-reaction energy IRC modeling are also in agreement with the literature of the impurity-doped anatase sensors, and may be used to tailor the sensor response to the requirements of industrial applications.

The response range of the sensor is characterized by the reducing gas concentration [CO(g)]* at which further increase in the gas concentration has minimal effect on the resistance. From Eq. (3), the resistance saturates when the number of liberated electrons N_{lib} becomes [CO(g)] independent. Examining Eq. (8a), this occurs when the second term, $(1 + K_{ox})\, K_{ads}$ [CO(g)], dominates the denominator. Since $K_{ox} << 1$ for the E_{ox} listed in Table I (Eq. 10b), the product K_{ads} [CO(g)] determines [CO(g)]*, meaning that the ratio of the adsorption reaction energy E_{ads} to the temperature T has an exponential effect on the response range. Therefore, a minimal variation in E_{ads}, such as that extracted for the anatase/La_2O_3/CuO sensor, significantly alters the response range (Fig. 7).

To quantify the change in the response range with E_{ads}, we determine [CO(g)]* at 500°C by calculating the relative resistance decrease, $(R_o - R)/R_o$ with increasing gas concentration; for the purposes of illustration, we use the criteria that R^* corresponds to the relative resistance decrease which is 90% of that at complete saturation, $(R_o - R_{sat})/R_o$ (Fig. 8a). A lowered value of [CO(g)]* may thus be achieved by adding dopants that lower the energy level of the adsorbed CO state, thereby increasing the negativity of E_{ads}. Since CO gas molecules are energetically favored to adsorb rather than desorb for negative E_{ads}, a more negative E_{ads} value results in added CO molecules available for oxidation with surface O^-. Our prediction of enhanced CO adsorption upon increasing the magnitude of E_{ads} is observed in XPS spectra of anatase surfaces doped with La_2O_3 and/or CuO [17].

From this result [CO(g)]* may be tailored to the specifications of an industrial application. For example, a dopant producing $E_{ads} \sim -0.39$ eV halves the relative response range, $|[CO(g)]^* - [CO(g)]^*_{doped}| / [CO(g)]^*$, of the anatase sensor at 500°C (Fig. 8b). The resulting *on/off sensor* is particularly desirable for automotive applications, where early detection of increased CO levels is important [6]. Conversely, dopants generating less negative E_{ads} produce a higher [CO(g)]*; in particular, modifying E_{ads} to ~ -0.30 eV doubles the relative response range. This can be important for industrial sensor applications in which an accurate reading of the CO gas concentration is needed, as is required in a fuel-fired furnace [6].

The sensitivity of the sensor is characterized by the resistance decrease, R_{sat}/R_o, at complete saturation, after which further increase in the gas concentration has no effect on the resistance. Since $N_{lib} \sim K_{ox} / (1 + K_{ox}) \sim K_{ox}$ at complete saturation, the sensitivity depends exponentially on the ratio of the oxidation reaction energy E_{ox} to the temperature T. As with the response range, a small variation of the oxidation reaction energy significantly alters the sensitivity; decreasing E_{ox} of the pure anatase sensor by several hundredths of an eV increases the sensitivity noticeably (Fig. 9). Given that adsorbed CO is energetically fa-

Table 1. Reaction energies for anatase-phase based TiO_{2-x} sensors (in eV).

	Anatase	Anatase / 10%wt La_2O_3	Anatase/ 10%wt La_2O_3 / 2%wt CuO
E_{ads} (adsorption of CO)	−0.34	−0.37	−0.39
E_{ox} (oxidation of CO)	0.22	0.28	0.25

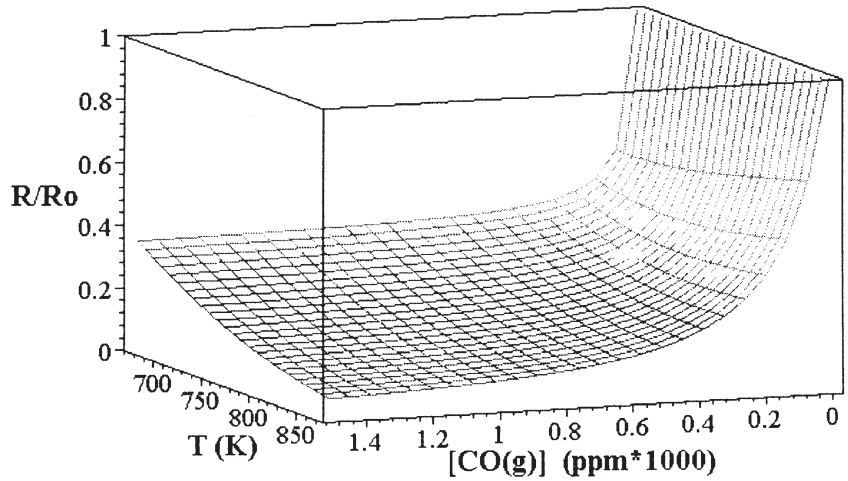

Fig. 7. Small variation of the adsorption reaction energy produces a considerable change in the response range of the sensor. Here $E_{ads} = -0.39$ eV and $E_{ox} = 0.22$ eV.

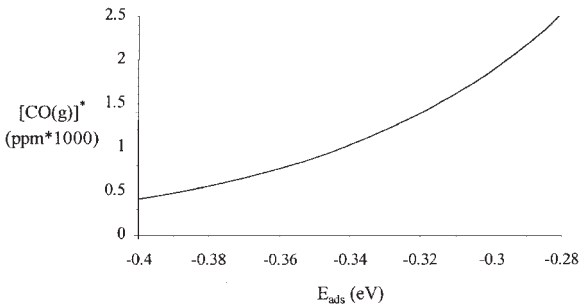

Fig. 8b. [CO(g)]* may be tailored to the specifications of an industrial application by modifying E_{ads}. $E_{ads} \sim -0.39$ eV halves the relative response range of the anatase sensor at $T = 773$ K, while $E_{ads} \sim -0.30$ eV doubles the relative response range.

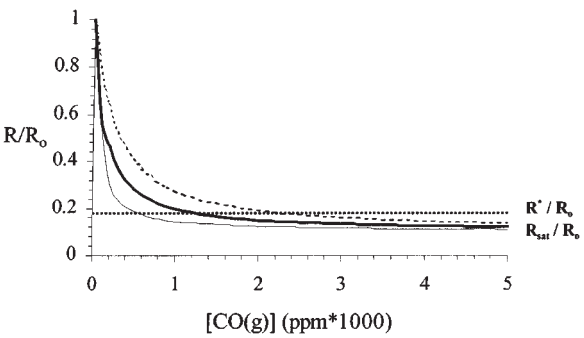

Fig. 8a. [CO(g)]* at $T = 773$ K for $E_{ads} = -0.29$ eV (dashed curve), $E_{ads} = -0.34$ eV (dark continuous curve), and $E_{ads} = -0.39$ eV (lighter continuous curve). [CO(g)]* produces R^* corresponding to the relative resistance decrease which is 90% of that at complete saturation, $(R_o - R_{sat})/R_o$. The IRC model predicts a lowered value of [CO(g)]* via dopants that increase the negativity of E_{ads}.

vored to remain non-oxidized for positive E_{ox}, reducing the oxidation reaction energy yields more oxidized (CO_2) molecules and hence liberated electrons. Thus modifications to E_{ox} have an appreciable effect on the sensitivity (Fig. 10a).

Our prediction of increased surface oxidation is observed upon adding dopants that alter E_{ox}. For instance, the anatase/La_2O_3 sensor, doped with La_2O_3 to help stabilize the anatase structure and retard the conversion of TiO_2 to its rutile phase [29], has a larger E_{ox} than the pure anatase sensor, which is consistent with observed lessened surface reactivities due to La_2O_3 inclusion. Conversely, the presence of CuO has been observed to promote the steady oxidation reaction, thus diminishing E_{ox} [17]. From this result E_{ox} may be adjusted via doping to produce the desired sensitivity. For example, a dopant generating $E_{ox} \sim 0.26$ eV triples R_{sat}/R_o at 500°C, while one which lowers E_{ox} to ~ 0.20 eV decreases R_{sat}/R_o by a factor of three (Fig. 10b). Experimental optimization of the sensor via the addition of dopants can now be theoretically predicted by adjusting the reaction energies in the IRC model.

We have also examined the validity of using the simpler one-reaction energy sensing mechanism derived in Section III.2, and find that the single-stage process within the IRC model is clearly unable to describe the qualitative experimental temperature dependence seen in the experimental data. In fact, using the best comparison ($E_1 = E_{ads} + E_{ox} = -0.12$ eV) between the one-reaction energy model and the ana-

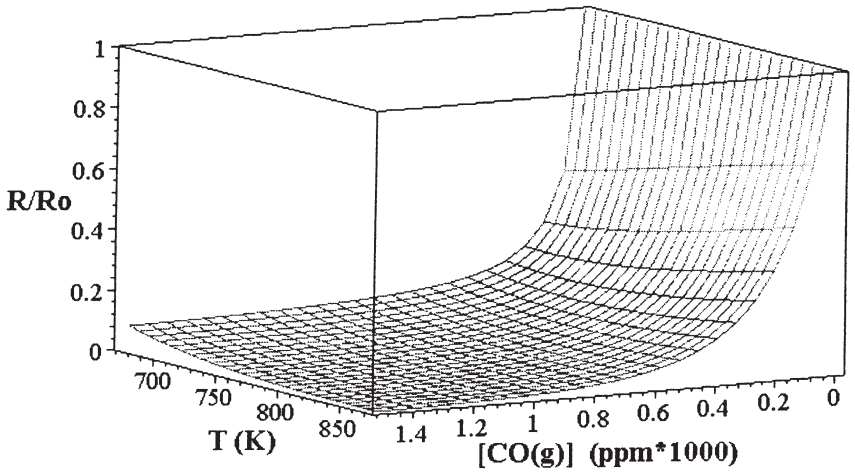

Fig. 9. A small decrease of the oxidation reaction energy obtained from Fig. 6 (here $E_{ads} = -0.34$ *e*V and $E_{ox} = 0.18$ *e*V) significantly increases the sensitivity of the sensor.

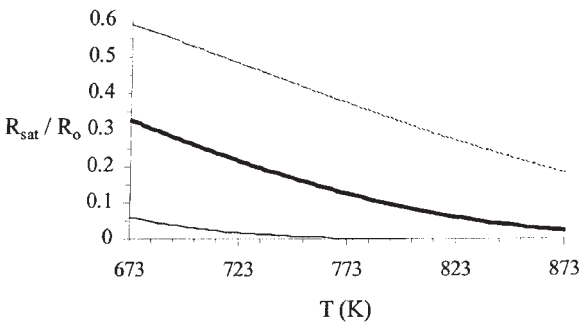

Fig. 10a. R_{sat}/R_o vs. T for $E_{ox} = 0.26$ eV (dashed curve), $E_{ox} = 0.22$ *e*V (dark continuous curve), and $E_{ox} = 0.18$ eV (lighter continuous curve). Reducing E_{ox} garners more oxidized (CO_2) molecules and hence liberated electrons, and thus has an appreciable effect on the sensitivity.

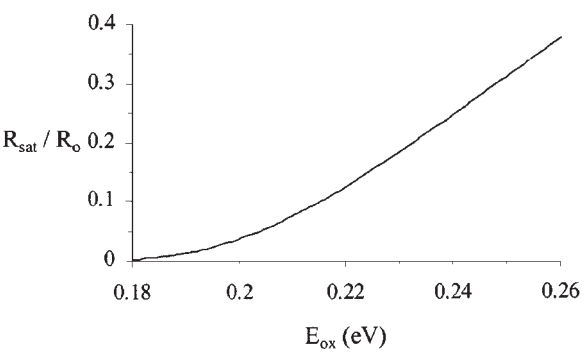

Fig. 10b. E_{ox} may be adjusted via doping to produce the desired sensitivity. $E_{ox} \sim 0.26$ eV triples R_{sat}/R_o at $T = 773$ K, while a dopant which lowers E_{ads} to ~ 0.20 eV decreases $R_{sat}/R\sim$ by a factor of three.

tase sensor data, the temperature dependence of R/R_o is opposite that of experiment at [CO(g)] = 1500 ppm (Fig. 11). The qualitative temperature dependence could be matched using a positive E_1, but only at the expense of describing the response range. With only one reaction energy, the single-stage mechanism is able to duplicate either the response range or the sensitivity, but not both. Therefore, because of this complexity of the sensor response, a two-reaction energy model is required to depict how dopants alter the kinetics of gas sensing.

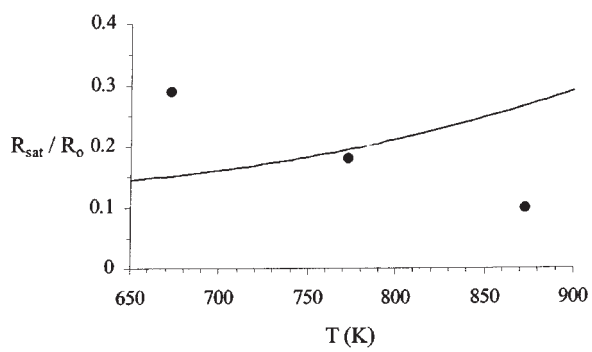

Fig. 11. Using the best comparison ($E_1 = E_{ads} + E_{ox} = -0.12$ *e*V) between the one-reaction energy IRC model (continuous line) and the anatase sensor data (data points), the temperature dependence of R/R_o is opposite that of experiment at [CO(g)] = 1500 ppm. With only one reaction energy, the single-stage mechanism is able to characterize either the response range or the sensitivity, but not both.

V. Effect of Microstructure on Optimizing Sensitivity

In addition to optimizing the response range and sensitivity via doping, the IRC model predicts novel sensing properties that depend on microstructural details of the sensor. Here we consider the effects on the sensitivity upon *1*) reducing grain size and *2*) controlling the neck area of the intergranular contacts.

1. Nanocrystalline Response (Reduced Grain Size)

Through the surface area to volume ratio contained in the calculation of the depletion layer width (Eqs. 2,3,8), the IRC model predicts a strong grain size dependence on the sensitivity. As mentioned earlier, depletion regions in nanocrystalline n-type ceramic sensors may extend throughout the entire composite prior to the introduction of the reducing gas, leading to a vanishing initial conducting fraction f_c. These n-type semiconducting materials of finer grain experience enhanced non-stoichiometry [30], with a total number of intrinsic electrons N_i given by $2x\rho\ V_g$, as discussed in Section III. Despite the increase in the intrinsic carrier concentration, a nanocrystal is nevertheless easily depleted of its intrinsic carriers. Using Eq. (8b), the total number of surface ions N_d is proportional to the product of the grain surface area A_g and the ion adsorption site concentration $[S_o]$. The ratio N_d/N_i therefore scales like a_o/xr_g, where r_g is the grain radius and a_o the lattice constant. From Eq. (2), the depletion layer thus spans the entire grain prior to reducing gas exposure for sufficiently small r_g; for example, ultra-fine grained n-type rutile ($x \sim 0.027$) is completely depleted for samples prepared with r_g less than 20 nm [30]. The conductivity of such a fully depleted composite is equal to σ_i.

However, nanocrystalline sensors are also likely to have their depletion regions removed by the reducing gas. From Eq. (8a) we see N_{lib} is proportional to the product $A_g[S_o]$. Consequently N_{lib}/N_i also scales like a_o/xr_g. As a result of Eq. (3), the depletion layer is completely replenished in ultra-fine grained composites, unlike their coarsened counterparts. The response of a nanocrystalline sensor is thus characterized by a dramatically increased sensitivity (Fig. 12). This enhanced response in nanocrystalline non-stoichiometric n-type ceramics, compared to the corresponding coarsened materials, has been observed in both CeO_2 [31] and SnO_2 [32].

2. Sensitivity of a Granular Microstructure (Controlled Neck Area)

In the previous discussion, we have applied the IRC model to a weakly sintered microstructure characterized by back-to-back Schottky barriers at the intergranular contacts. In general, though, the grain packing in a ceramic green compact is non-uniform. Depending on the characteristics of the starting powder and the sintering schedule, the resulting weakly sintered granular microstructure might possess as many open and closed 'necks' (Fig. 13) as activated Schottky barrier type of grain-grain contacts, with the former having

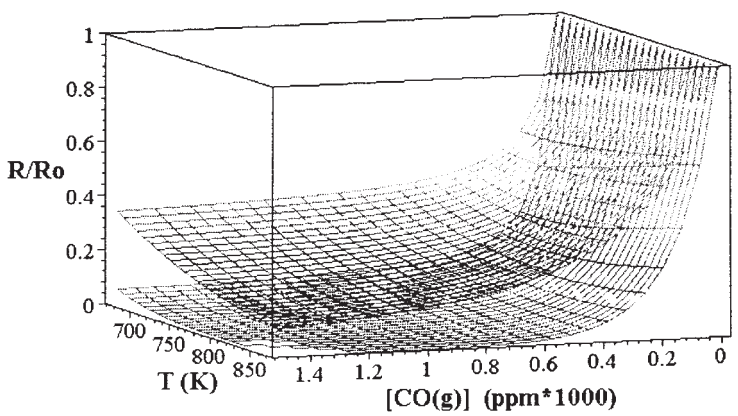

Fig. 12. The sensor is characteristically more sensitive for smaller grain sizes (lower continuous grid) vs. coarsened grains (upper continuous grid) with a ten times greater radius.

ohmic resistances significantly smaller than those of the latter [20].

The open necks are exemplified by a depletion zone that exists only on the periphery of the neck, but does not extend to the center. Consequently, the conducting bulk phase is able to percolate between the neighboring grains, such that the intergranular conductance is largely that of the non-depleted bulk region in the center of the neck. By contrast, in the case of a closed neck, the depletion zone extends across the full area of the neck, resulting in a higher resistance path between the grains [20,33]. The closed neck geometry arises either because less complete sintering leaves a narrower neck, or from excess surface oxygen ions increasing the depletion layer thickness such that the conduction channel is pinched off. However, if the expanded depletion region and neck widths are comparable, the conductance becomes very sensitive to variations in the surface charge. In this circumstance, a reducing gas is capable of re-opening the neck by replenishing the depletion layer, thereby significantly decreasing the intergranular resistance in a manner analogous to the operation of n-type ZnO adsorption-effect transistors [34].

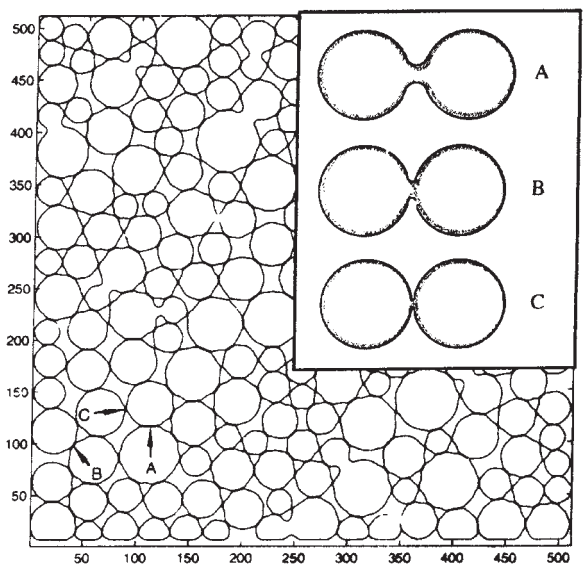

Fig. 13. Depending on the characteristics of the starting powder and the sintering schedule, the resulting granular microstructure might possess (*a*) open and (*b*) closed 'necks', as well as (*c*) activated Schottky barriers. Because the depletion zones that develop on the periphery of (*a*) do not overlap, the intergranular conductance is largely that of the non-depleted bulk region in the center of the neck, resulting in a lower resistance path than in (*b*) and (*c*).

In a granular ceramic sensor microstructure, therefore, the closed necks (and the Schottky barrier contacts) with their higher resistance control the conduction process until the fraction of open necks f_c increases above the percolation limit. Above the percolation threshold f_p, we would expect conduction paths across the sample to develop through open necks, such that the conductivity quickly increases to that of the open neck/bulk region [20]. In a sensor with f_c initially less than f_p, the transition from constricted to open neck conduction may occur upon introduction of the reducing gas, provided there is a suitable distribution of closed necks with widths comparable to the depletion length. The gas-surface reaction kinetics corresponding to the surface charge variation may still be calculated using the two-reaction energy IRC modeling. For the electrical transport, however, the high conductivity component (the open necks) is now symmetrically (or randomly) distributed rather than coated by the more insulating regions (the closed necks and Schottky barrier contacts). Therefore, the unsymmetrical EMT in Eq. (1) must be replaced with a theory that properly incorporates the behavior near the percolation transition. Accordingly, the effective medium conductivity σ_{eff} near f_p is calculated using the general effective media (GEM) equation [35]

$$\frac{f_c\left(\sigma_c^{1/t}-\sigma_{eff}^{1/t}\right)}{\sigma_c^{1/t}+\left(\frac{1-f_p}{f_p}\right)\sigma_{eff}^{1/t}}+\frac{(1-f_c)\left(\sigma_i^{1/t}-\sigma_{eff}^{1/t}\right)}{\sigma_i^{1/t}+\left(\frac{1-f_p}{f_p}\right)\sigma_{eff}^{1/t}}=0 \qquad (13)$$

where σ_c and σ_i are the conductivities of open and closed necks, respectively. This more general approach, which allows for non-spherical components, is characterized by the percolation threshold f_p and a percolation exponent *t*, which may be obtained from experiment or numerical simulation. Recent studies using the GEM equation have found that both f_p and *t* decrease and the electrical conductivity curve becomes steeper as the aspect ratio of the conducting component increases [36–39]. For the purpose of relating the kinetics of the gas-surface reactions to conduction through the granular ceramic, we choose typical three-dimensional morphology parameters $f_p = 0.16$ and $t = 1.7$ [37].

Using IRC reaction kinetic modeling together with the GEM equation, the sensitivity of a ceramic sensor

to a reducing gas is found to depend strongly on the initial open neck fraction. Consider a microstructure with f_c just below f_p, and containing a number of closed necks with widths comparable to the depletion length. Upon CO exposure, the reducing gas re-opens these necks to increase f_c above f_p such that a transition to open neck conduction occurs, which is exemplified by the enhanced sensitivity (Fig. 14a). On the other hand, if initially f_c is above f_p, the sensor resistance already approaches that of a conducting open neck. Consequently the change in resistance with CO introduction is minimal, and such a microstructure is not useful for sensing (Fig. 14b).

The symmetrical IRC model, by relating variations in surface charge around closed necks to the conduction through a granular microstructure, can be utilized to predict properties of granular sensors analogous to adsorption-effect transistors. Thus, control of the

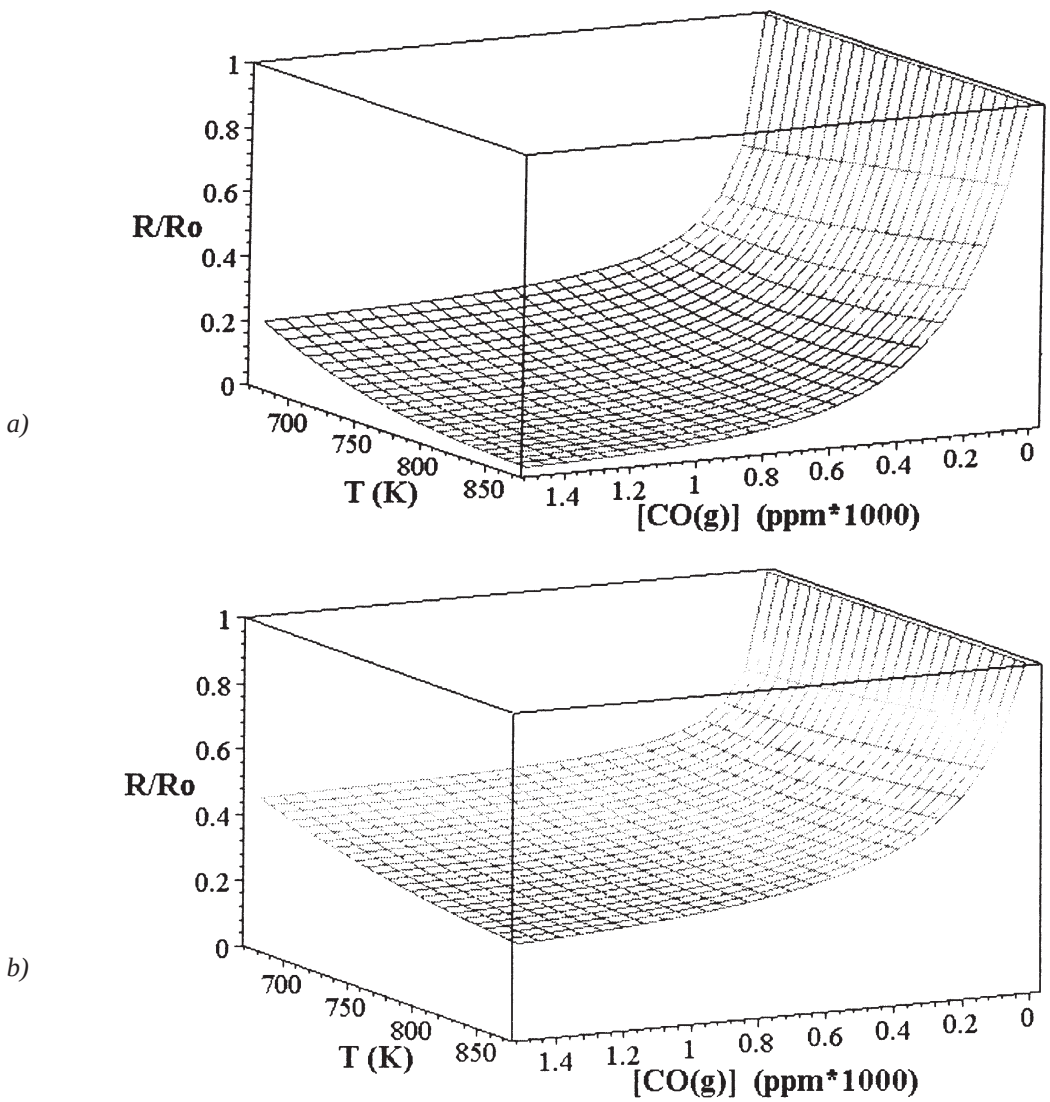

Fig. 14. A sensor with a granular microstructure registers *a*) an enhanced sensitivity if the initial open neck fraction is below the percolation threshold (here $f_{c,initial} = f_p - 0.05$), but *b*) weaker sensitivity when f_c is above f_p (here $f_{c,initial} = f_p + 0.05$) since the sensor resistance is already comparable to that of the open necks prior to reducing gas exposure. The resistance is calculated using IRC reaction kinetic modeling with the same parameters as Fig. 6 ($E_{ads} = -0.34$ *e*V, $E_{ox} = 0.22$ *e*V) and the GEM equation for the granular microstructure.

microstructure can be used to optimize sensor properties, serving as an alternative to doping in improving the sensitivity.

In this section, we have used the IRC model to elucidate the strong sensitivity dependence on the details of the microstructure. Since the reaction energies determine the temperature dependence of the response, we may compare the effects on the sensitivity of various microstructural parameters by fixing E_{ads} and E_{ox}. Fig. 15 compares the change in the sensitivity with grain size (Fig. 12) and neck area (Figs. 14a and 14b) at 500°C.

VI. Summary

A simple relation between the reaction energies of the sensing mechanism and the sensing behavior of n-type oxide sensors has been established through the integration of surface reaction kinetics and electrical conduction in two component media. Specifically, the resistance of a metal oxide gas sensor has been calculated using the Integrated Reaction Conduction (IRC) model, which is parameterized by the depletion layer width of the oxide grains.

We have developed an explicit mapping to integrate the standard effective medium picture with a more mesoscopic treatment of the phase field microstructure. The conducting volume fraction in the IRC model has been calculated in terms of the reducing gas concentration and temperature using a two-reaction energy kinetic method. Its scope was found to depend on the concentrations of surface oxygen ions producing the depletion layer and liberated electrons replenishing the depletion layer via the reducing gas.

Through a comparison with experimental data of the sensor resistance, the adsorption and oxidation reaction energies for anatase-phase based TiO_{2-x} sensors were extracted. The IRC model also predicts several additional features of the gas sensor. Adding dopants that decrease the magnitude of the adsorption reaction energy generates an increased response range; improved sensitivity is afforded by dopants that decrease the oxidation reaction energy. Moreover, the sensitivity is enhanced for reduced grain sizes, and is also realized in granular microstructures, provided that the conducting open neck fraction is below the percolation threshold prior to reducing gas exposure.

By understanding the effects of dopants, temperature, grain size and sintering on the sensor response, the IRC model allows us to improve the design of electroceramic gas sensors.

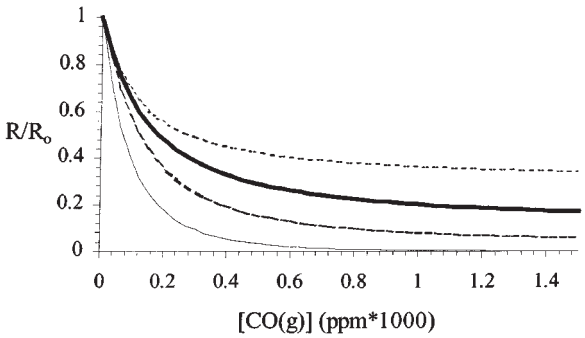

Fig. 15. The IRC model predicts a strong sensitivity dependence for the anatase sensor (dark continuous curve) upon changing its microstructural details, including reducing the grain size (lighter continuous curve), and generating a granular microstructure initially below its percolation threshold (dashed curve) and above its percolation threshold (dotted curve). Here $T = 773$ K.

Acknowledgements

We gratefully acknowledge financial support by the NSF Center for Industrial Sensors and Measurements under grant EEC-9523358 (BC and BP) and NSF grant DMR-9703044 (YW). It is a pleasure to acknowledge useful discussions with A. Kazaryan, P.K. Dutta, Z. Liang, N.O. Savage, C.Ciobanu and S.A. Akbar.

References

1. S.A. Akbar and C.C. Wang, *The Electrochemical Society Interface*, **5,** 41 (1990).
2. B.C.H. Steele, Editor, *Electronic Ceramics* (Elsevier, New York, 1991).
3. P.T. Moseley, *Sensors and Actuators B,* **6,** 149 (1992).
4. A.M. Azad, S.A. Akbar, et al., *J. Electrochem. Soc.*, **139,** 3690 (1992).
5. R. N. Blumenthal, J. Coburn, J. Baukus, and W.M. Hirth, *J. Phys. Chem. Solids*, **27,** 643 (1966).
6. J.A.S. Ikeda, Y.-M. Chiang, and C.G. Madras, in *Ceramic Transitions, Vol. 24, Point Defects and Related Properties of Ceramics,* T.O. Mason and J.L. Routbort, eds. (American Ceramic Society, Cincinnati, OH, 1991), p. 341.
7. J.A.S. Ikeda and Y.-M. Chiang, *J. Am. Ceram. Soc.,* **76,** 2437 (1993).

8. J.A.S. Ikeda, Y.-M. Chiang, A.J. Garratt-Reed, and J.B. Vandersande, *J. Am. Ceram. Soc.*, **76,** 2447 (1993).
9. C.R.A. Catlow and R. James, *Proc. R. Soc. London A,* **384,** 157 (1982).
10. U. Balachandran and N.G. Eror, *J. Mater. Sci.*, **23,** 2676 (1988).
11. P.G. Harrison and M.J. Willett, *J. Chem. Soc., Faraday Trans. 1,* **85,** 1921 (1989).
12. Y. Shimizu and M. Egashira, *MRS Bulletin,* **24,** 18 (1999).
13. N. Taguchi, Japanese Patent Application No. 45-38200 (1962); Y. Shimizu, Y. Nakamura, and M. Egashira, *Sensor and Actuators B,* **13–14,** 128 (1993).
14. T. Seiyama, A. Kato, K. Fujiishi, and N. Nagatani, *Anal. Chem.*, **34,** 1502 (1962); S. Saito, M. Miyayama, K. Koumoto, and H. Yanagida, *J. Am. Ceram. Soc.*, **68,** 40 (1985).
15. J.D. Plummer and P.B. Grifin, *Nuclear Instruments and Methods in Physics Research B,* **102,** 160 (1995).
16. Y. Wang, Y. Liu, C. Ciobanu, and B. R. Patton, "Simulating Microstructural Evolution and Electrical Transport in Ceramic Gas Sensors," submitted to *J. Am. Ceram. Soc.*
17. P.K. Dutta, et al., *J. Phys. Chem. B,* **103,** 4412 (1999).
18. P.T. Moseley and D.E. Williams, in *Techniques and Mechanisms in Gas Sensing,* P.T. Moseley, J.O.W. Norris, and D.E. Williams, eds. (Adam Hilger, Bristol, England, 1991), p. 47; V. Lannto and P. Romppainen, *Surf. Sci.* **192,** 243 (1987).
19. D.A.G. Bruggeman, *Ann. Phys. (Leipzig),* **24,** 636 (1935); R. Landauer, *AIP Conference Proceedings,* **40,** 2 (1977).
20. D.E. Williams, in *Solid State Gas Sensors,* P.T. Moseley and B.C. Tofield, eds. (Bristol, 1987), p. 92.
21. L.Q. Chen and Y. Wang, *JOM,* **48,** 13 (1996).
22. W. Gopel, G. Rocker, and R. Feierband, *Phys. Rev. B,* **28,** 3427 (1983).
23. J. Watson, K. Ihokura, and G. Coles, *Meas. Sci. Technol.,* **4,** 711 (1993).
24. J. Steinfeld, J. Francisco, and W. Hase, *Chemical Kinetics and Dynamics* (Prentice-Hall, Inc., New York, 1989), p. 21.
25. K. Laidler, *Chemical Kinetics* (McGraw-Hill, Inc., New York, 1987), p. 263.
26. L.E. Reichel, *A Modern Course in Statistical Physics* (John Wiley & Sons, Inc., New York, 1998), p. 241.
27. E. Garrone, V. Bolis, B. Eubini, and C. Morterra, *Langmuir,* **5,** 892 (1989); C. Morterra, *J. Chem. Soc., Faraday Trans. 1,* **84,** 1617 (1988).
28. H.W. Gundlach and K.E. Heusler, *Z. Phys. Chem. N.F.,* **119,** 213 (1980).
29. S. Hishita, I. Mutoh, K. Koumoto, and H. Uanagida, *Ceram. Int.,* **9,** 61 (1983).
30. C.D. Terwilliger and Y.-M. Chiang, *J. Am. Ceram. Soc.,* **78,** 2045 (1995).
31. J.Y. Ying and A. Tschöpe, *Chem. Eng. J.,* **64,** 225 (1996).
32. C. Xu, J. Tamaki, N. Miura, N. Yamazoe, and Denki Kagaju, **58,** 1143 (1990).
33. N.M. Beekmans, *J. Chem. Soc. Faraday Trans. I,* **74,** 31 (1978).
34. M. Nakagawa and H. Mitsudo, *Surf. Sci.*, **175,** 157 (1986).
35. D.S. McLachlan, M. Blaszkiewicz, and R.E. Newnham, *J.Am. Ceram. Soc.*, **73,** 2187 (1990).
36. J.Y. Yi and G.M. Choi, *J. Electroceramics,* **3,** 361 (1999).
37. J. Kovacik, *Scripta. mater.,* **39,** 153 (1998).
38. J.J. Wu and D.S. McLachlan, *Physica A,* **241,** 360 (1997).
39. D.S. McLachlan, *Physica B,* **254,** 249 (1998).